CORRECTION POSTED 6 MARCH 2024; SEE FULL TEXT

MICROROBOTS

Human-scale navigation of magnetic microrobots in hepatic arteries

Ning Li[1,2]*†, Phillip Fei[1,2]†, Cyril Tous[1,2]†, Mahdi Rezaei Adariani[1,2,3], Marie-Lou Hautot[1,2], Inès Ouedraogo[1,4], Amina Hadjadj[1,2], Ivan P. Dimov[1,2]‡, Quan Zhang[5,6]*, Simon Lessard[1,2], Zeynab Nosrati[7], Courtney N. Ng[7], Katayoun Saatchi[7], Urs O. Häfeli[7], Charles Tremblay[8], Samuel Kadoury[1,8], An Tang[1,2,9], Sylvain Martel[8,10]*, Gilles Soulez[1,2,9]*

Using external actuation sources to navigate untethered drug-eluting microrobots in the bloodstream offers great promise in improving the selectivity of drug delivery, especially in oncology, but the current field forces are difficult to maintain with enough strength inside the human body (>70-centimeter-diameter range) to achieve this operation. Here, we present an algorithm to predict the optimal patient position with respect to gravity during endovascular microrobot navigation. Magnetic resonance navigation, using magnetic field gradients in clinical magnetic resonance imaging (MRI), is combined with the algorithm to improve the targeting efficiency of magnetic microrobots (MMRs). Using a dedicated microparticle injector, a high-precision MRI-compatible balloon inflation system, and a clinical MRI, MMRs were successfully steered into targeted lobes via the hepatic arteries of living pigs. The distribution ratio of the microrobots (roughly 2000 MMRs per pig) in the right liver lobe increased from 47.7 to 86.4% and increased in the left lobe from 52.2 to 84.1%. After passing through multiple vascular bifurcations, the number of MMRs reaching four different target liver lobes had a 1.7- to 2.6-fold increase in the navigation groups compared with the control group. Performing simulations on 19 patients with hepatocellular carcinoma (HCC) demonstrated that the proposed technique can meet the need for hepatic embolization in patients with HCC. Our technology offers selectable direction for actuator-based navigation of microrobots at the human scale.

INTRODUCTION

Techniques enabling targeted navigation of micro- or nanorobots in arteries through external actuation sources are being implemented for diagnosis, targeted therapy, and intervention (*1*–*6*). Current approaches for delivering local therapy in interventional radiology are often invasive and require highly skilled operators. For example, to treat advanced hepatocellular carcinoma (HCC), the third leading cause of cancer-related deaths worldwide (700,000 deaths/year), transarterial chemoembolization (TACE) is the preferred approach (*7*). TACE using drug-eluting beads (DEBs) can simultaneously embolize arteries and deliver chemotherapy drugs. Biodegradable DEBs allow sustained release of antineoplastic agents while maintaining local drug concentrations and staying within the therapeutic range with reduced potential for hepatotoxicity (*8*, *9*). However, DEBs need to be injected supraselectively into tumor-feeding arteries under fluoroscopy, which remains a technical challenge on a human scale. Besides the possibility of technical failure to reach the arterial feeder of the tumor, visualization of the tumor and assessment of complete tumor coverage under fluoroscopy after embolization are challenging (*10*, *11*).

The use of field forces generated by external actuators to navigate biocompatible microrobots in the deeper arteries (>70-cm-diameter range) of large animals is an interesting alternative but challenging because of the weak field force, overwhelming drag force of blood flow, and gravity (*12*–*16*). Two main approaches are commonly used today to increase the steering success rate: using larger robots and reducing the distance between the robot and the actuator. Larger robots have the advantage of providing greater physical-field forces but are not suitable for targeting complex vascular structures because they are unable to penetrate small vessels (*17*, *18*); for example, in fluoroscopy-guided DEB-TACE, DEBs between 100 and 300 μm have ideal penetration into HCC and smaller ones can cause liver complications (*8*, *19*). Reducing the distance between the robot and the actuator can provide enough force to navigate untethered micro- or nanorobots in the fast bloodstream, but the method cannot be applied in deep arteries (>70-cm-diameter range) (*20*, *21*). Optical methods, for example, are generally limited to superficial layers because of their poor ability to penetrate biological tissues (≤7 cm depth) (*22*, *23*), and acoustic actuators are only effective for controlling foreign particles inside small-organism vasculatures or superficial layers (*13*, *24*). Current magnetic navigation techniques using electromagnets and permanent magnets as actuators are only used in in vitro experiments, limbs, heads, superficial organs, or small animals such as mice and rabbits because the magnetic field strength of the dipole field is proportional to the dipole moment and inversely proportional to the cube of the distance (*14*, *20*, *21*, *25*–*30*). For biocompatible superparamagnetic materials like iron oxide nanoparticles, achieving a saturation magnetization level that induces the

---

[1]Clinical Laboratory of Image Processing (LCTI), Centre de Recherche du Centre Hospitalier de l'Université de Montréal (CRCHUM), Montréal, Québec H2X 0A9, Canada. [2]Université de Montréal, Montréal, Québec H3T 1J4, Canada. [3]Inria, Palaiseau 91120, France. [4]Université de Nantes, Nantes 44035, France. [5]School of Mechatronic Engineering and Automation, Shanghai University, Shanghai 200444, China. [6]School of Artificial Intelligence, Shanghai University, Shanghai 200444, China. [7]Faculty of Pharmaceutical Sciences, University of British Columbia, Vancouver, British Columbia V6T 1Z3, Canada. [8]Department of Computer Engineering and Software Engineering, Polytechnique Montréal, Montréal, Québec H3T 1J4, Canada. [9]Centre Hospitalier de l'Université de Montréal (CHUM), Montréal, Québec H2X 0C1, Canada. [10]Department of Bioengineering, McGill University, Montréal, Québec H3A 0E9, Canada.
*Corresponding author. Email: ning.li@polymtl.ca (N.L.); lincolnquan@shu.edu.cn (Q.Z.); sylvain.martel@polymtl.ca (S.M.); gilles.soulez.med@ssss.gouv.qc.ca (G.S.)
†These authors contributed equally to this work.
‡Present address: Massachusetts General Hospital, 55 Fruit Street, Boston, MA 02114, USA.

maximum force due to the magnetic gradients typically requires a minimum magnetic field strength of approximately 1.5 T (*31*). However, it is difficult to achieve this for other magnetic platforms [beyond magnetic resonance imaging (MRI) platforms] where the gradients decrease rapidly with increasing distance. In such cases, it becomes challenging to attain such saturation levels at deeper locations within the body, specifically within a 70-cm-diameter range. In addition to magnetic field intensity, the rapid decrease in magnetic field gradients with distance further weakens the magnetic field force acting on the magnetic microrobots (MMRs).

We previously proposed to navigate MMRs through the arteries with a 1.5-T MRI scanner to perform selective arterial embolization, a technique that has been called magnetic resonance navigation (MRN) (see fig. S1) (*18*). Although MRI vendors claim to have gradients reaching 45 mT/m, in reality it is limited at the maximum of 43 mT/m for 23% duty cycle or 20 mT/m at 45% duty cycle (*12*). Over the past decade, this patented technology has been demonstrated in rabbits (*32*) and pigs (*18*). However, the in vivo experiments are limited by using insert gradient coils [15-cm bore size, 400-mT/m gradients (*32*)] or by using a large-scale robot [1.5-mm-diameter ferromagnetic bead (*18*)]. Furthermore, the gravitational force of the MMRs is greater than the buoyancy force, and the net force (gravity − buoyancy) is approximately equivalent to the force produced by a magnetic gradient of 71.85 mT/m in a 3-T MRI scanner (*12*, *33*), which is greater than the maximum MRI steering gradient of clinical MRI scanners (45 mT/m). Theoretical calculations and in vitro experiments have revealed that when the target vessel branch angle is +20° above the horizontal plane, the MRN force yields a navigational success rate of ≥70%, and the success rate declines rapidly as the angle increases further (*12*). Moreover, high-velocity blood flow (≥40 cm/s in the common hepatic artery of pig or human) induces a greater challenge for microrobot navigation (*34*). Therefore, MRN using MMRs, with significance testing, has yet to be demonstrated in human or large animal models.

Although MRI systems (Connectom MRI scanners, $N = 4$) equipped with ultrahigh gradients (up to 300 mT/m) exist, their primary use is for brain studies because of the limited bore size (56 cm) (*35*). These systems come with additional challenges, such as heat dissipation, peripheral nerve stimulation, and safety considerations, that limit their clinical use.

To overcome the above problem, this paper reports an algorithm to determine the optimal patient position that will favor gravity toward the target vessel branch; that is, gravity does not negatively affect navigation but acts as an additional navigational force to make navigation easier. We present a feasibility study in 12 pigs showing that MRN of MMRs is possible when combined with gravitational forces. We believe that the proposed technique can improve the efficiency of various target-navigation techniques based on external actuators, including but not limited to magnetic navigation.

RESULTS

Experimental workflow

Figure 1 describes the experimental design. Before the experiments, iron oxide superparamagnetic nanoparticles, which are visible on T1-weighted MR images, were encapsulated into a biocompatible polymer that was made from biodegradable and US Food and Drug Administration–approved poly(lactic-*co*-glycolic acid) (PLGA) (see Supplementary Materials). Because our experiments were designed to evaluate the feasibility of the proposed targeting technology, the MMRs were not loaded with chemotherapeutic drugs. However, successful loading of MMRs with the anticancer drug doxorubicin has been previously reported (*32*).

A balloon catheter was placed selectively in the main hepatic artery under fluoroscopy from a femoral approach. The distal branches of the hepatic vascular tree can be obtained from the segmentation of contrast images using cone-beam computed tomography (CBCT) and three-dimensional (3D) digital subtraction angiography (DSA). Volumetric images were acquired in supine (0°), lateral right (90°), prone (180°), and lateral left (270°) positions (Fig. 1A, example of supine position). Then, we examined the range of body rotation angle, specifically pathways that favor gravity toward the targeted liver lobe [the right lateral + caudate lobes (RLL + CL), the right medial lobe (RML), the left medial lobe (LML), or the left lateral lobe (LLL)], while ensuring that α (Fig. 1B) remained less than 0. Here, α is the angle between the horizontal plane (HP) and the targeted branch leading to the tumor at the vessel bifurcation. A detailed algorithm and a flowchart (see Materials and Methods) to determine the optimal body rotation angle are provided.

Once optimally positioned, the pig was transferred from the angiography room table to the MRI patient table using a docking table to maintain its optimal position. The balloon lumen was connected to a high-precision MR-compatible inflation device (see Materials and Methods) to reduce the flow velocity from ~40 to ~8 cm/s for MRN (Fig. 1C) (*34*).

After controlling the flow, the lumen of the catheter was connected to a specifically designed MMR injector (see Supplementary Materials) capable of forming suitable particle aggregates and injecting them automatically. When an MMR aggregate was released from the injector, MR imaging gradients were activated in the proper direction (see Supplementary Materials) to direct the aggregate to the target lobe (Fig. 1C). Basic principles of MRN were presented in the Supplementary Materials. Serial T1-weighted volumetric interpolated breath-hold examinations (T1-VIBE) were acquired to assess the distribution of MMR aggregates in the target and nontarget lobes every five injections. After all MMR injections were completed (100 injections), the pig was removed from the MRI field. Outside the magnetic field, the aggregates broke up into individual particles and reached the distal arterioles of the target. Then, the animals were moved back into the MRI bore. T1-VIBE images were acquired, and the corresponding postprocessing method (see Supplementary Materials) was executed to assess the distribution of MMR aggregates in the target and nontarget lobes. A flowchart illustrating the experimental procedure for MRN is provided in fig. S2.

MMR synthesis and injection

There were two main steps in the fabrication of MMRs: producing the superparamagnetic nanoparticles (Fig. 2A) and encapsulating them into the PLGA material (Fig. 2B). The iron oxide nanoparticles (12 ± 3.6 nm) were coated with biocompatible C_{12}-bisphosphonate. The nanoparticles had a saturation magnetization of 70 emu/g (weight = 1 mg, number of measurements = 1, room temperature; see fig. S3) (EV9, Microsense) and accounted for 60% of the total weight of MMRs (mass density = 2.95 g/cm^3). The MMRs (number of microrobots = 54, weight = 1.01 mg, number of measurements = 1, room temperature) showed no hysteresis at 0 T and were thus truly superparamagnetic, with a magnetization saturation value at 2 T of 36 emu/g (EV9, Microsense) (Fig. 2C). MMRs were not cytotoxic to

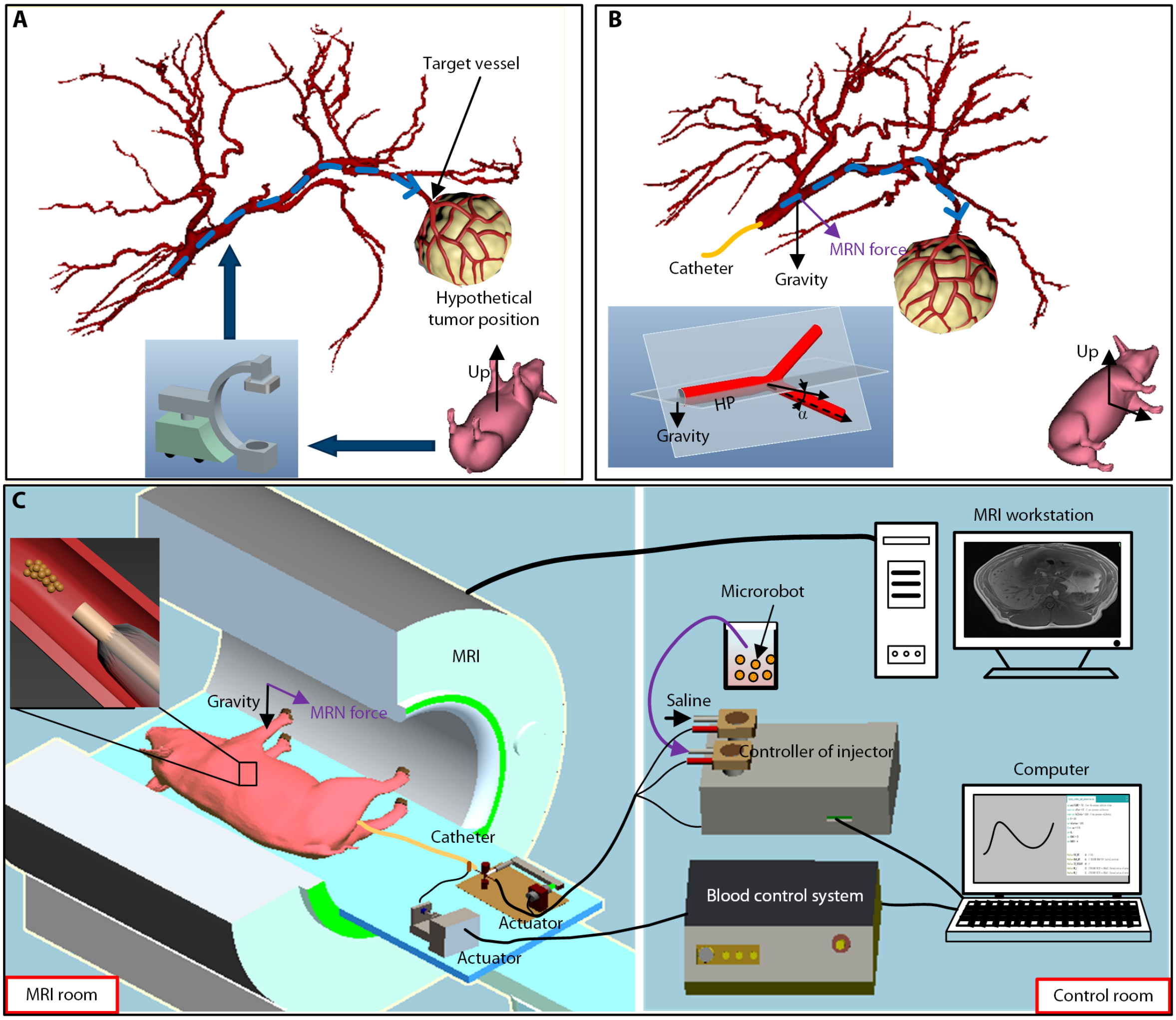

Fig. 1. Schematic of microrobot navigation in vivo. (**A**) CBCT acquisition was used to obtain the 3D model of the vascular tree. (**B**) After processing the pathways relative to the horizontal plane to assess the effect of gravity on the target operation, the pig was rotated accordingly. (**C**) Once placed in the compatible position for MRN, the hepatic flow was reduced by partially inflating a balloon catheter using a high-precision MRI-compatible balloon inflation system. The microrobot injector, connected to the catheter, created and released a single-particle aggregate with the desired number of particles. After release, the imaging gradients of MRI were activated to steer the aggregate into the target vessels.

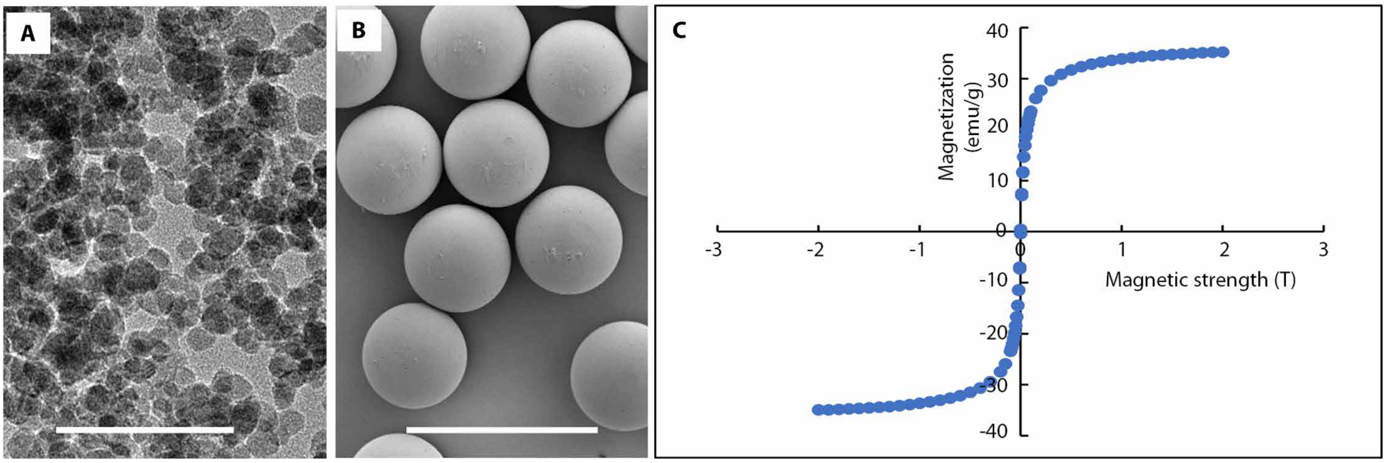

Fig. 2. Magnetic microrobots used in the experiments. (**A**) Transmission electron microscope micrograph of the iron oxide magnetic nanoparticles. Scale bar, 50 nm. (**B**) Scanning electron microscope image of the MMR. Scale bar, 500 μm. (**C**) Magnetization curve of the MMR.

human embryonic kidney cells and human umbilical vein endothelial cells (Lonza, Walkersville, MD, USA) when examined by direct and indirect cell viability and proliferation assays. Detailed information on MMR fabrication and biocompatibility testing is available in (*36*).

The number of MMRs per injection was controlled by the particle injector (Fig. 1C), and the number determined the size of MMR aggregates (*31*). The internal diameters of the left and right hepatic arteries are 3.0 ± 0.3 mm and 3.6 ± 0.4 mm, respectively (*37*). The criteria for determining the optimum number of MMRs per aggregate were to maximize the number of particles injected in a single injection while keeping the size of the aggregates smaller than the diameters of the left and right hepatic arteries. Therefore, the number of particles per aggregate was limited to 20 to form an aggregate length of 1.3 to 2.1 mm, resulting in 20 ± 6 particles injected each time (*31*). The distal branches were less than 2 mm.

Microrobot injection in the absence of the magnetic field

Two living pigs were enrolled to examine the control distribution of MMRs in the liver when injected under fluoroscopy in an angiography room without MRN and aggregate formation. For each pig, 2000 MMRs were released directly into the pig's proper hepatic artery via a 4-French catheter, and then the liver was harvested and imaged with T1-VIBE images. As shown in Fig. 3, most of these particles were evenly distributed in all four liver lobes (RLL + CL, RML, LML, and LLL). The particles were mainly concentrated in the peripheral areas of the liver, indicating that they embolized small arteries and arterioles.

Predicting the optimal body position angle

A total of 12 pigs were randomly divided into three groups: the control group (pigs #1 to #4) receiving MMR injection without MRN in a supine position, the right-navigation (R-navigation) group (pigs #5 to #7), and the left-navigation (L-navigation) group (pigs #8 to #12). The R-navigation group targeted RLL + CL (pigs #5 and #6) and RML (pig #7). The L-navigation group targeted LML (pigs #8 and #9) and LLL (pigs #10 to #12).

We developed an algorithm and a flowchart (see Materials and Methods) to determine the optimal patient position that will favor gravity toward the target vessel branch. In Fig. 4, we present the calculation results, which show the range of optimal body rotation angles obtained based on different vascular trees (Fig. 4, A and C) for targeting different liver lobes (Fig. 4, D to G) in pig #8. For all other seven pigs in the navigation groups, the vessel segmentation and the optimal rotation angles, similar to the results in Fig. 4 (B and D to G), are given in figs. S4 to S10. The single optimal body rotation angle for each individual pig, corresponding to the targeted liver lobe mentioned above, has been provided below along with the MRN targeting effect.

After rotating the pigs to their single optimal body rotation angles, they were immobilized on the docking table and transferred to the MRI suite. Once in the MRI, magnetic resonance angiography (MRA) was used to acquire the hepatic vascular tree.

Blood flow control

In previous work, we showed that a high flow rate reduces the efficiency of MRN because the weak magnetic steering forces do not have enough time to deflect the aggregate toward the target lobe during the short transit time (*38*). On the other hand, low flow can cause microrobots to stick to the bottom of the blood vessels due to gravity and friction. Our previous studies have shown that the blood flow rate in the main hepatic artery should be in the range of 0.5 to 1.0 ml/s to optimize MRN (*12*, *34*).

For the L- and R-navigation groups, the hepatic flow rate was controlled by partially inflating a balloon catheter positioned in the proximal proper hepatic arteries. The infusion volume increment to the balloon was set to 0.01 ml. Each time the measured blood pressure value decreased by 2 mmHg, the blood flow was measured until the desired flow rate of ~0.5 to 1.0 ml/s was obtained.

Figure 5 illustrates the procedure for measuring the blood flow rate. Flow rates were measured from cine phase-contrast images at the cross section of the proper hepatic artery. Free flow (no balloon inflation) was determined at 3.3 ± 2.3 ml/s ($N = 12$, all pigs), and controlled flow was 0.7 ± 0.3 ml/s ($N = 8$, two navigation groups) after balloon inflation.

MRN experiments and postprocessing of the experimental results

After blood flow control (for the MRN groups) and MRA, 100 MMR aggregates with 20 ± 6 particles per aggregate were injected into the liver of each pig through the coaxial lumen of the balloon catheter. When a particle aggregate was released from the injector's actuator (Fig. 1), the MRN sequence was turned on for 30 s to ensure that the magnetic force was applied to the MMR aggregate during the entire transit time until it reached the targeted lobe. For the two navigation groups, the direction and amplitude of the magnetic gradients are described in the Supplementary Materials.

After MMR injections were completed, the pigs were removed from the MRI field for 30 s and then moved back. Artifact locations were verified on T1-VIBE images (Fig. 6A). To better identify the distribution of these artifacts, the 3D hepatic vessel tree segmented on CBCT images was rigidly co-registered on the segmented MRA images (Fig. 6B) using 3D-Slicer (version 4.11.20200930) (*39*). This allowed particle distribution to be analyzed on the basis of the volume of the artifacts and their relative spatial relationship to the hepatic artery and four hepatic lobes, as shown in Fig. 6 (C to E). Comparing Fig. 3C (MMR injection under fluoroscopy) with Fig. 6C [MMR aggregate injection in MRI without steering (control group)], MMRs had evenly distributed over four liver lobes in the absence of MRN regardless of the presence of the magnetic field.

The analysis of particle distributions in different groups indicated that the proposed navigation method substantially increased targeting efficiency. The proportion of particles entering the right liver lobes increased from 47.7 ± 8.8% (control group) to 86.4 ± 3.5% (R-navigation group), with a two-tailed *P* value of 0.0018. Similarly, the proportion of particles entering the left liver lobes increased from 52.2 ± 8.8% (control group) to 84.1 ± 11.7% (L-navigation group), with a two-tailed *P* value of 0.0054. Further details on the particle distribution can be found in Table 1.

The proportion of particles in individual lobes was also examined. In the control group, the proportion of particles entering the RLL + CL, RML, LML, and LLL was 24.3 ± 5.2%, 23.4 ± 8.0%, 31.9 ± 12.3%, and 20.4 ± 9.7%, respectively; the corresponding values increased to 61.5 ± 15.8% (pigs #5 and #6), 40.8% (pig #7), 75.3 ± 24.1% (pigs #8 and #9), and 52.9 ± 12.9% (pigs #10 to #12) when the four lobes were targeted separately. Therefore, the number of MMRs reaching four different target liver lobes had a 1.7- to 2.6-fold increase in the navigation groups, compared with the control group. Detailed targeting results were provided in table S1. On the basis that the results of the R- and L-navigation are statistically

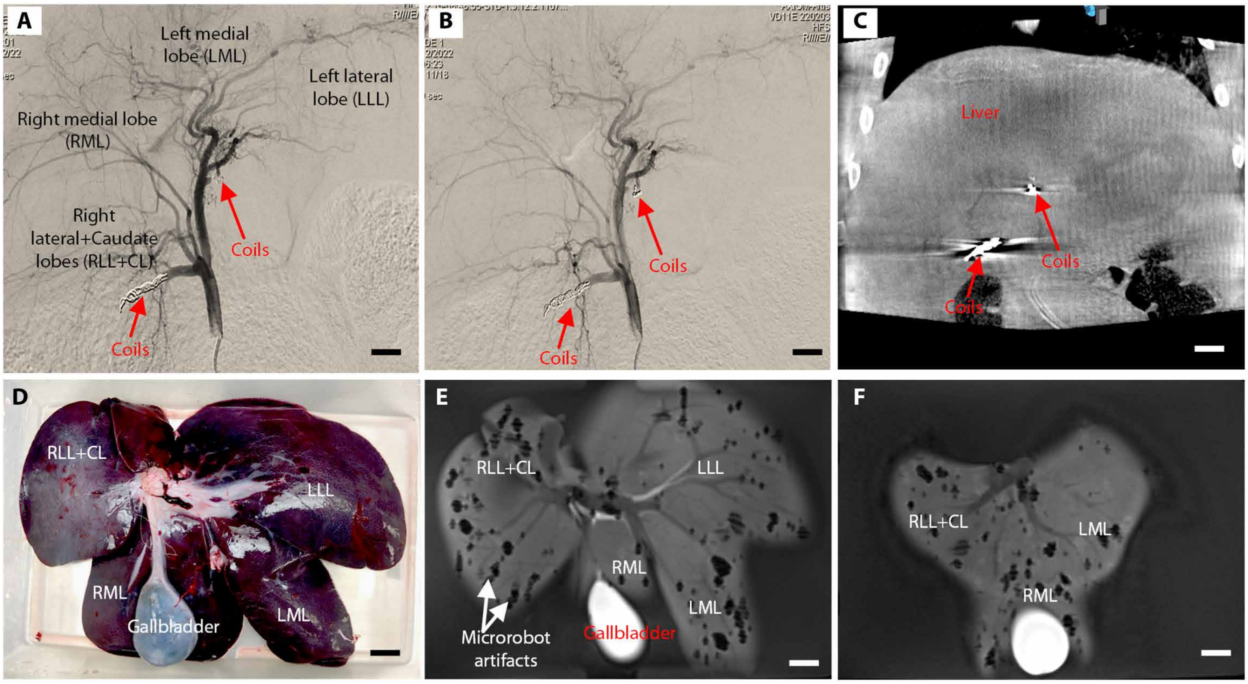

Fig. 3. Liver distribution of MMR after injection in the angiography room without magnetic field. (**A**) Angiography showing the anatomy of the liver before embolization. The left gastric and gastroduodenal arteries were embolized with coils before the injection of the microrobots to prevent embolization in the stomach or duodenum. Scale bar, 1 cm. (**B**) DSA acquisition after microrobot injection showing no evidence of flow occlusion and no visibility of microrobots. Scale bar, 1 cm. (**C**) CBCT showing no visibility of microrobots. Only the coils positioned in left gastric and gastroduodenal arteries are visible (arrows). Scale bar, 1 cm. (**D**) Gross pathology with the caudal view of liver lobes annotated in white. Scale bar, 1 cm. (**E** and **F**) Particle distributions in two slices of the T1-VIBE images of (D). Scale bars, 1 cm (E and F).

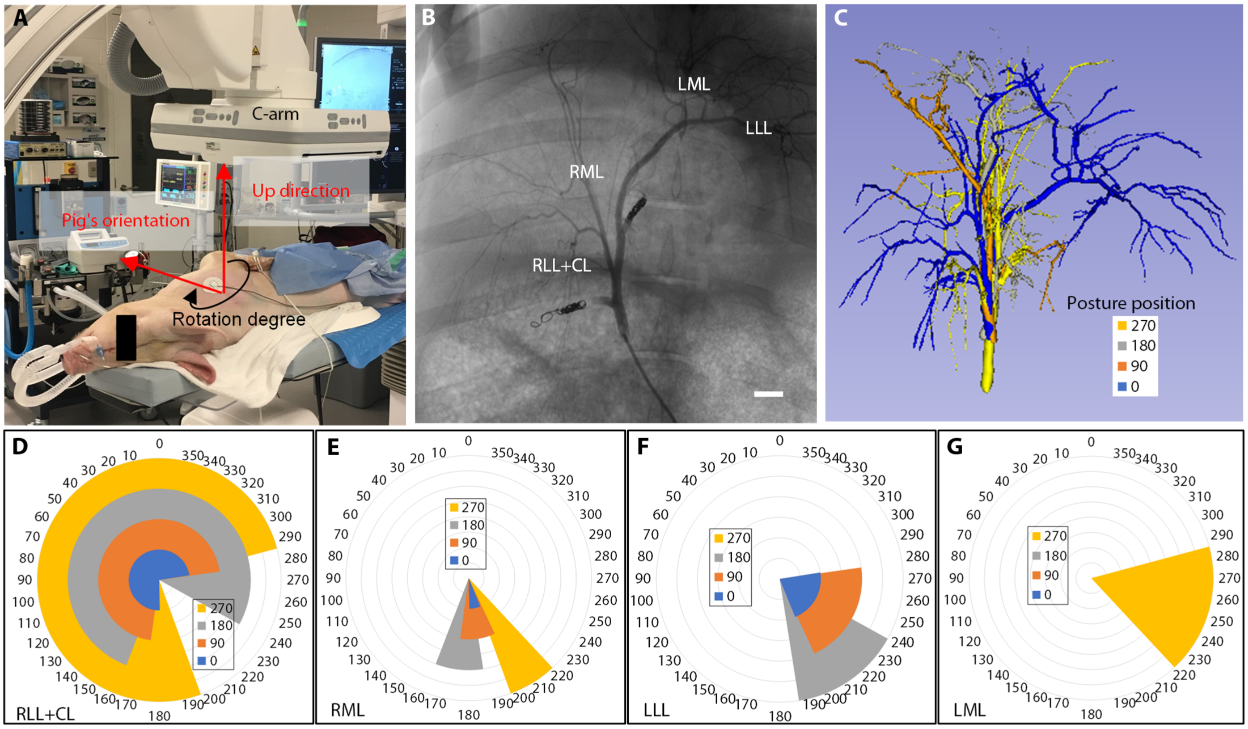

Fig. 4. Workflow for obtaining the optimal rotation angles targeting different liver lobes. (**A**) Vascular trees were imaged at different posture positions in the angiography room, here in the lateral left position. (**B**) DSA of the hepatic vascular artery was obtained when the pig was in the supine position. Scale bar, 1 cm. (**C**) The segmented vascular tree was registered at four different positions when the proper hepatic artery was aligned. (**D** to **G**) Compatible angular ranges that can reach (D) RLL + CL, (E) RML, (F) LLL, and (G) LML depending on the pig's posture (individual color); values in the box indicate the postural rotation angles when imaging the vascular tree.

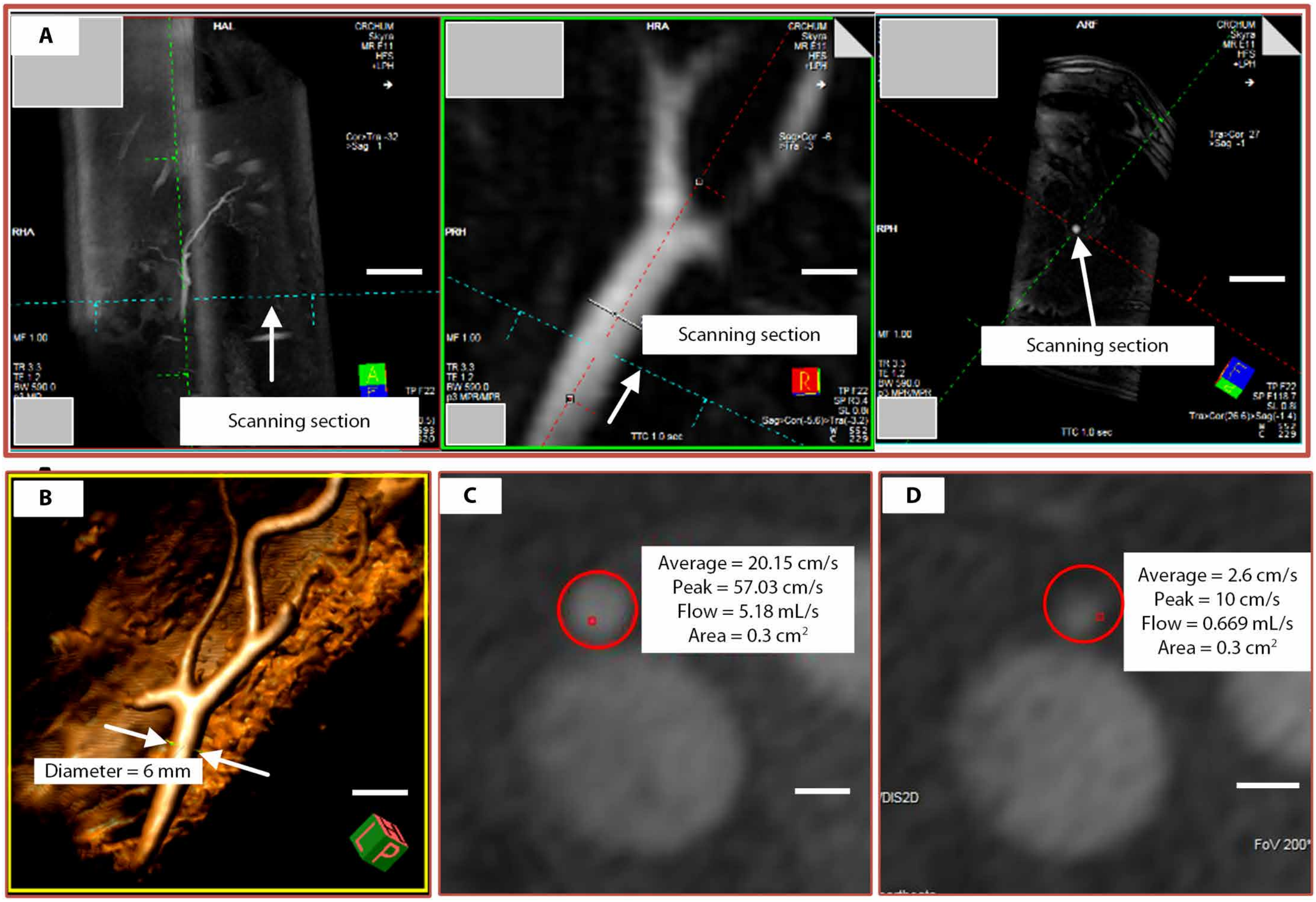

Fig. 5. Procedure for controlling and measuring blood flow. (**A**) Localization procedure for cross-sectional flow measurements in the proper hepatic artery. Scale bars, 5 cm (left), 5 mm (middle), and 5 cm (right). (**B**) 3D reconstruction of the blood vessel structure for vessel diameter measurements, and flow measurements by the 2D cine phase-contrast sequence before (**C**) and after (**D**) blood flow control. Scale bars, 1 cm (B) and 5 mm (C and D).

significant compared with the control group ($P < 0.05$), we can specify a targeted lobe (RLL + CL, RML, LML, or LLL) to further improve the targeting efficiency of MMRs in the tumor areas.

In addition to the targeting effect, the disintegration of MMR aggregates into smaller aggregates or individual MMRs after leaving the magnetic field region was also examined. Pig #12 was used for verification. The results (fig. S11) indicated that there were indeed some MMR aggregates that would break down in the liver after leaving the MRI magnetic field.

Simulation in an atlas of human liver anatomy

An atlas of 19 patients who had undergone a TACE in 2018/2019, some with multifocal HCCs representing a total of 32 nodules, was used to determine whether the tumor distribution was compatible with the proposed MRN approach to reach the tumor. According to the Michels classification of hepatic artery anatomy (*40*), these patients have type 1 anatomy in 79% of cases ($N = 15$), as shown in Table 2. Two out of the 19 patients are type 2, one patient is type 3, and one patient is type 5. The location of HCC nodules regardless of the liver classification predominates in the medial lobes.

From this atlas, we determined the number of bifurcations that can be crossed over the total number of bifurcations to reach the tumor, based on our proposed algorithm. Figure 7 shows an example of an HCC patient from the atlas. If the patient is lying on the right side (optical patient position between 22° and 110°), the first three bifurcations toward the target branch can be crossed. The last bifurcation (fourth) cannot be reached regardless of the patient's position.

Two bifurcations are generally sufficient to reach the left lobe nodules (segments II, III, and IV). To reach the right lobe nodules, three bifurcations are usually sufficient. Basically, if there is a nodule in the left lobe, the patient should be in a prone position or on the left side. For right-sided nodules, a supine position was generally more appropriate, except for segment VIII, which required a right-sided position. At the optimal body position obtained by our proposed algorithm, 78% (25 of 32) of HCC nodules (see Table 2) can be targeted, provided that all vessel bifurcations leading to the targeted lobe favor gravity during MRN. There were only two cases where the bifurcation elevation angle (α, see Fig. 1B) was above 20°, respectively at 23° and 36.5°. Therefore, only 2 of 32 HCC nodules (6.2%) were unreachable by this method. Only with such a small proportion of nodules, the proposed MRN procedure would have no additional therapeutic effect.

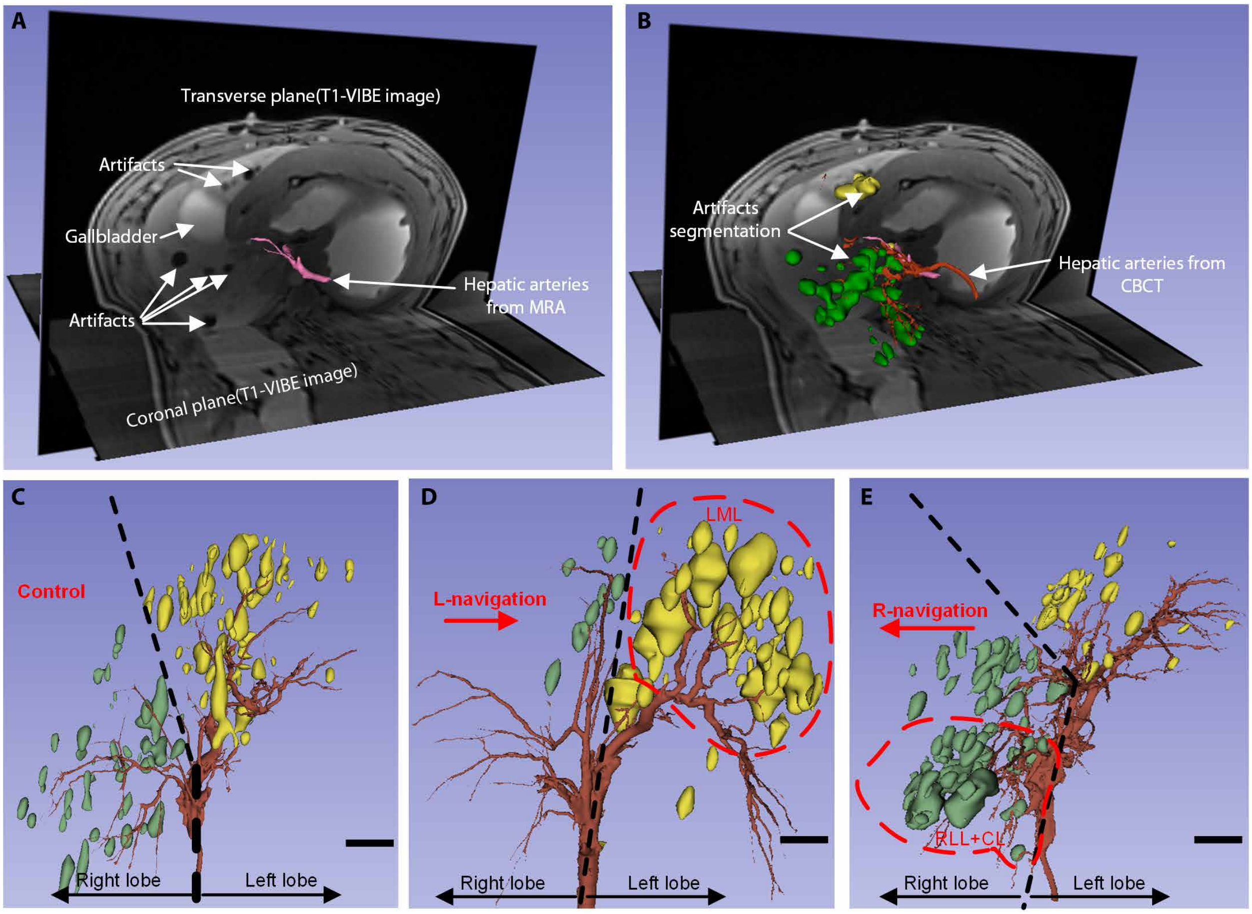

Fig. 6. Quantification and 3D localization of microrobot-induced artifacts in pigs. (**A**) Identification of artifacts in the T1-VIBE sequence and segmentation of the hepatic arterial tree (pink) from MRA data. (**B**) Coordinate alignment of the MRA (pink) and CBCT (dark red) images and segmentation of artifacts (yellow and green). (**C** to **E**) Identification of the artifacts in pigs #3, #8, and #6, respectively, after inserting the 3D hepatic vascular tree extracted from the CBCT; artifacts of MMR in the left liver are shown in yellow and in the right liver in green. Scale bars, 1 cm (C to E).

Table 1. Optimal body rotation angle and microrobot distributions. This table presents the optimal body rotation angle for each pig and the resulting microrobot distributions after the target operation.

Groups	Pig #1	Pig #2	Pig #3	Pig #4	Pig #5	Pig #6	Pig #7	Pig #8	Pig #9	Pig #10	Pig #11	Pig #12
Pig rotation angle												
Control	0°	0°	0°	0°								
R-navigation					140°	50°	130°					
L-navigation								240°	210°	270°	250°	250°
Distribution ratio of particles to the targeted liver lobe (%)												
Control*	52.4	45.7	34.5	58.3								
R-navigation					89.9	87.7	81.7					
L-navigation								99.5	80.2	72.9	71.4	96.3

*In the control group, the distribution ratio of particles is given for the right liver lobes.

DISCUSSION

We demonstrated the feasibility of navigating MMRs to target a specific lobe of the liver in clinical MRI using a balloon catheter placed in the proper hepatic artery for flow control, a custom-purpose MMR injector to generate MMR aggregates, magnetic steering forces generated by the imaging gradient of a clinical MRI, and an algorithm that can predict the optimal body position to favor the effect of gravity during MRN.

Although several systems have been proposed for propelling microrobots in vivo, these systems are generally limited to small animals or specific regions of the body because of weak actuator-based field forces. Clinical translation of these technologies to

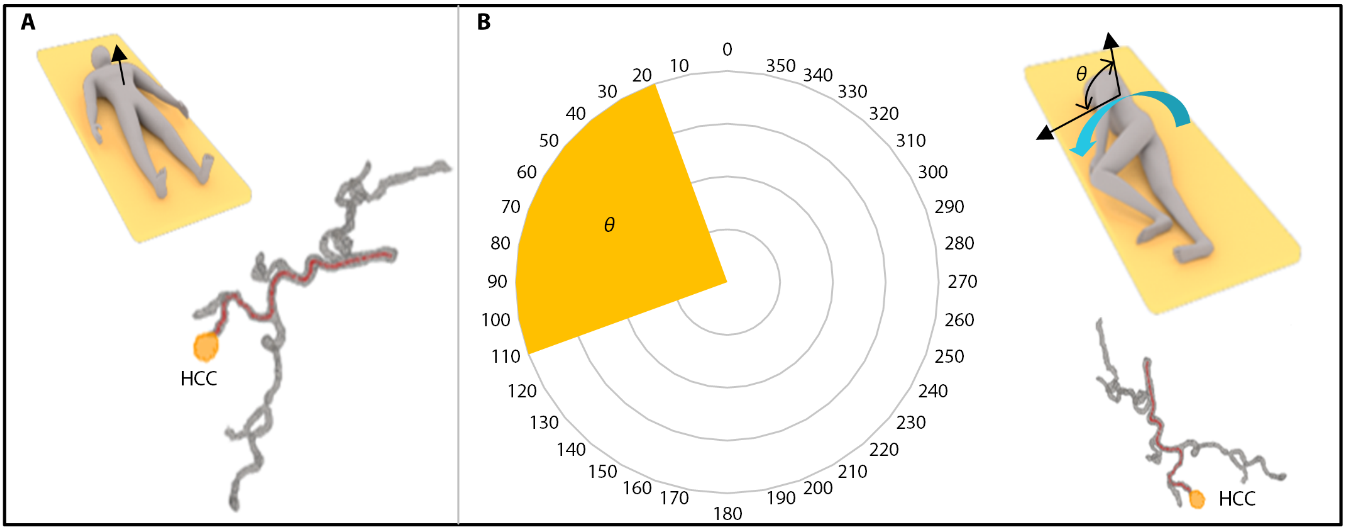

Fig. 7. Simulation of MRN in an atlas of human liver anatomy with the proposed algorithm. (**A**) For a patient with a nodule in segment VIII, four vascular bifurcations need to be crossed; however, in the supine position, microrobot navigation can be influenced by gravity. (**B**) Our proposed algorithm recommends patient positioning on the right side, using the microrobot's gravity to facilitate targeted MRN.

Table 2. HCC and bifurcation crossings. Locations of HCCs in 19 patients and the number of bifurcations that need to be crossed to reach them. Individual HCCs with the number of bifurcations that can be crossed with the elevation angle below the horizontal plane after optimal positioning (numerator), out of all bifurcations that need to be crossed (denominator). The percentage of all tumors in the same segment that can be targeted successfully by crossing all bifurcations is presented in the last row. ID, identification; F, female; M, male; N/A, not applicable.

Patient ID	Segment with HCC							Anatomy type	Sex
	II	III	IV	V	VI	VII	VIII		
#1		2/2			3/4	4/4		1	M
#2			2/2	4/4	4/4	2/4		1	M
#3							2/3	1	M
#4						4/4		1	F
#5		2/2						1	F
#6							3/3	2	M
#7	2/2							1	M
#8			1/1					3	F
#9			2/2					1	M
#10					3/3			1	M
#11	2/2		2/2	3/4				1	M
#12				3/3			2/3	1	M
#13			2/2					1	M
#14						3/3		5	M
#15		2/3						1	M
#16		2/2						1	M
#17				4/4				1	M
#18				1/1	2/3	3/3	2/2	2	M
#19	3/3	2/2	2/2					1	M
Patient number	3	5	6	5	4	5	4	N/A	N/A
Success to reach the tumor	100%	80%	100%	80%	50%	80%	50%	N/A	N/A

humans requires the ability to navigate microrobots at the human scale, which is possible by using clinical MRI with its human-sized imaging gradient coils to steer MMRs within the human vascular network. The 1.5- or 3-T main magnetic field of the MRI fully magnetizes superparamagnetic nanoparticles within the MMR (*41*). MRI is the most sensitive imaging modality to detect HCC or liver metastasis (*42*, *43*). In addition, the T1-VIBE sequence allows for the imaging and 3D localization of MMR because of the magnetic artifacts they produce on MRI acquisitions (*44*), enabling quantification of their distribution. This is a notable advantage compared with current fluoroscopy-guided DEB-TACE, where DSA in combination with or without CBCT cannot confirm complete tumor coverage after embolization (*11*).

Previous studies on the steering of MMRs identified fast blood flow as a major limitation of MRN (*34*). The blood flow in the liver arteries ranges between 3 and 4 ml/s. To be compatible with MRN, the flow rate was reduced to approximately 0.7 ml/s by precisely inflating an occlusion balloon catheter in the proximal proper hepatic artery with a dedicated inflation device. Using phase-contrast sequences was very convenient to monitor the flow during MRN experiments.

In a clinical setting, an implantable port can be easily inserted percutaneously into the proper hepatic artery with a dual-lumen catheter for balloon inflation, allowing DEB-TACE to be performed in the MR unit without hospitalization and subsequent catheterizations (*45*). This approach also allows the staging of DEB-TACE procedures with minimal morbidity.

Performing simulations of our approach on our small database of 19 TACE patients showed that the proposed approach was viable in over 94% of HCC nodules. Regardless of the nodule's location, one-third of them could be reached within two bifurcations (Table 2). Other locations requiring three to four bifurcations could be reached after the initial MRN followed by disaggregating the MMRs by removing the patient from the MRI. In humans, there are up to 10 types of vascular anatomies in the liver. The wide range of optimal rotation angles confirmed that several angular positions could access the targeted liver lobe, which means that the body could be positioned with slight angular variations while maintaining the reproducibility of the pathways that reached the desired lobe. Knowing the angular range with the proposed framework informs MRN planning and its potential success. A narrow angle with a limited range would leave very little room for positional error. The selection of the target lobe was random and not based on the principle of easiness. The experimental results revealed a statistical significance between the control group and the two experimental groups.

Limitations and future directions

In our study, the target nodule was positioned in favor of gravity, and the gradient's coordinates were defined as a single continuous direction toward the target hepatic branch. To further improve selectivity, knowing the location of the MMR artifact within the vascular tree could allow us to update the gradient to steer it toward the next target branch. Because of the small number of experimental animals limited to 12, our study is underpowered for statistical significance analysis of steering success to each of the four liver lobes.

The number of particles injected should be determined on the basis of the specific patient's needs and therapeutic threshold. In our experiments, each pig received a total of 2000 MMRs. As the number of particles reaching the target blood vessels increases, the blood flow rate to the branch decreases and, theoretically, the possibility that the particles might not reach the target vessel also increases. Excessive particle injection can therefore lead to nontarget embolization and cause adverse events. To overcome these limitations, further studies are necessary to determine the upper number of MMRs that should be administered.

The MMRs used in the experiment consist of PLGA and superparamagnetic nanoparticles. PLGA, widely used as a base material for drug and/or cell encapsulation, is biocompatible and biodegradable. Iron oxide nanoparticles, 5 to 20 nm in size, can be phagocytosed and cleared after microrobot decomposition without any negative or toxic effects, making them safe to use in living organisms (*32*, *46*). The microrobots can be loaded with doxorubicin or other antitumor drugs but were not loaded in our experiments for safety reasons and to save on cost (*32*). Further evaluation of the characteristics of the MMRs is necessary after drug loading. Lowering the MMR mass density to match that of blood is indeed a potential approach to minimize the influence of gravity and enable more efficient propulsion in liquid environments (*47*, *48*). However, there are certain challenges and considerations associated with this approach. If the goal is to match the mass density of blood, the microrobot materials should also be biocompatible to ensure safe interaction with biological systems. Compatibility with the surrounding environment and potential cytotoxicity issues must be carefully addressed. It is also important to note that the movement of microrobots within arterial blood flow entails complex vascular structures and blood flow dynamics. Reducing the concentration of magnetic nanoparticles inside MMRs to match the density of blood may result in a decrease in magnetic field forces (propulsion force). Whether the diminished driving forces can effectively cope with the challenges posed by the intricate blood flow patterns remains to be demonstrated. In our use of the MMRs, the combined propelling force, consisting of gravity, buoyancy, and MRN force, is relatively large because of the robot's density being approximately three times that of blood.

MMR tracking is achievable but not used in the article. If the tracking procedure occupies a duty cycle within the entire MRN process, it can lead to a decrease in the average gradient amplitude, which in turn may affect the targeting effectiveness. This contradicts our initial intention of maximizing the targeting force. The T1-VIBE sequence was used for MMR imaging, which is a postprocessing step performed after particle injection. In the experiment, we performed T1-VIBE imaging every five injections to assess the targeting effect of the MMRs. Although this evaluation involved a rough visual inspection of the artifact positions caused by the MMRs, we could not provide an analysis of the particle distribution as accurate as the time-consuming postprocessing performed after the procedure. Currently, we have explored the use of T1-VIBE and deep learning for automated analysis of particle distribution (*49*). The entire process takes several minutes, with the potential for further optimization to reduce the required assessment time. Although it is not a real-time tracking process, it will be sufficient to detect the occurrence of nontarget embolization of proximal blockage of segmental arteries and modify the MRN parameters if needed.

Our MRN experiments involve three main variables: blood control, body orientation optimization, and MRN force. Further validation is needed to assess the impact of various combinations of variables, such as with flow control and MRN but without orientation optimization, on the effectiveness of the target.

Clinical translation

In a clinical workflow, computed tomography angiography or 3D DSA acquisitions in four positions (0°, 90°, 180°, and 270°) are required to minimize errors associated with elastic deformation of the hepatic arteries induced by patient rotation in the MRN position. This can be done during the installation of the implantable arterial port. In addition, it may be helpful to consider using computational flow modeling techniques in combination with particle transport algorithms to simulate the effects of the flow drag force and the magnetic and gravitational forces on MRN performance (*50*). These simulations are useful to optimize blood flow and patient positioning during MRN. They can also be used to estimate the transit time of the aggregates between each bifurcation and to synchronize directional sequences with different angles.

The targeting approach we proposed is likely to be directly applicable to humans. First, both pigs and humans exhibit a similar alignment of the common hepatic artery, which primarily follows the length of the body or the $\mathbf{B}_0$ (main magnetic field of MRI) direction when inside an MRI bore. Second, the structure of the hepatic artery (vascular system) in pigs bears a high degree of resemblance to that in humans (*51*). Many similarities, including the vascular structure, have led to ongoing scientific exploration regarding the feasibility of liver xenotransplantation from pigs to humans. However, it is important to acknowledge that there may still be some differences between pig and human physiology, and further research and validation in human models are necessary to fully ascertain the applicability of these findings.

The navigation method proposed here has several advantages in clinical applications. In cases of liver embolization, MRN eliminates the need for repeated invasive catheterizations. Because MMR-TACE with MRN requires a hepatic arterial port, it is compatible with multimodal therapy. MMR-TACE can be combined with an intra-arterial infusion of chemotherapeutic drugs to facilitate the treatment of advanced-stage disease. It can also be combined with therapeutic agents injected intra-arterially, for example, oncolytic viruses (*52*) and immune checkpoint inhibitors (*53*); MMR-TACE with MRN is a localized treatment that improves efficacy while reducing morbidity and healthy tissue at risk. Last, MMRs can also be loaded with a new generation of drugs (tyrokinase inhibitors) (*54*, *55*).

MATERIALS AND METHODS

The experimental design involved using MRN in conjunction with an algorithm to achieve targeted navigation of MMRs in the bloodstream in vivo. The algorithm was proposed to predict the optimal body position with respect to gravity during endovascular microrobot navigation. As mentioned in Results, two pigs were enrolled to examine the control distribution of MMRs in the liver under fluoroscopy without MRN, MRI magnetic field region, and MMR aggregate formation, and an additional 12 pigs were used in the targeted navigation testing and randomly divided into three groups: a control group ($N = 4$), an R-navigation group ($N = 3$), and an L-navigation group ($N = 5$). Each pig received 100 injections of MMR aggregates.

MMR synthesis, specifically designed systems, and MRN sequence

The synthesis of MMRs, the MRI-compatible MMR injection system, and the optimization of the MRN sequence have been reported, and we briefly introduce them in the Supplementary Materials.

High-precision MRI-compatible balloon inflation system

A custom-made, piezoelectrically actuated, MRI-compatible balloon inflation system was used. The system was mainly divided into two parts, an MRI-compatible actuator near the scanner and a controller in the control room. A piezoelectric rotatory motor (diameter: 45 mm, thickness: 25 mm, made at Nanjing University of Aeronautics and Astronautics, China) was fitted to the actuator to accurately control the plunger flange of a syringe (3-ml syringe, with Becton, Dickinson and Company) forward and backward, controlling the inflation and deflation of the balloon catheter with an injection accuracy of

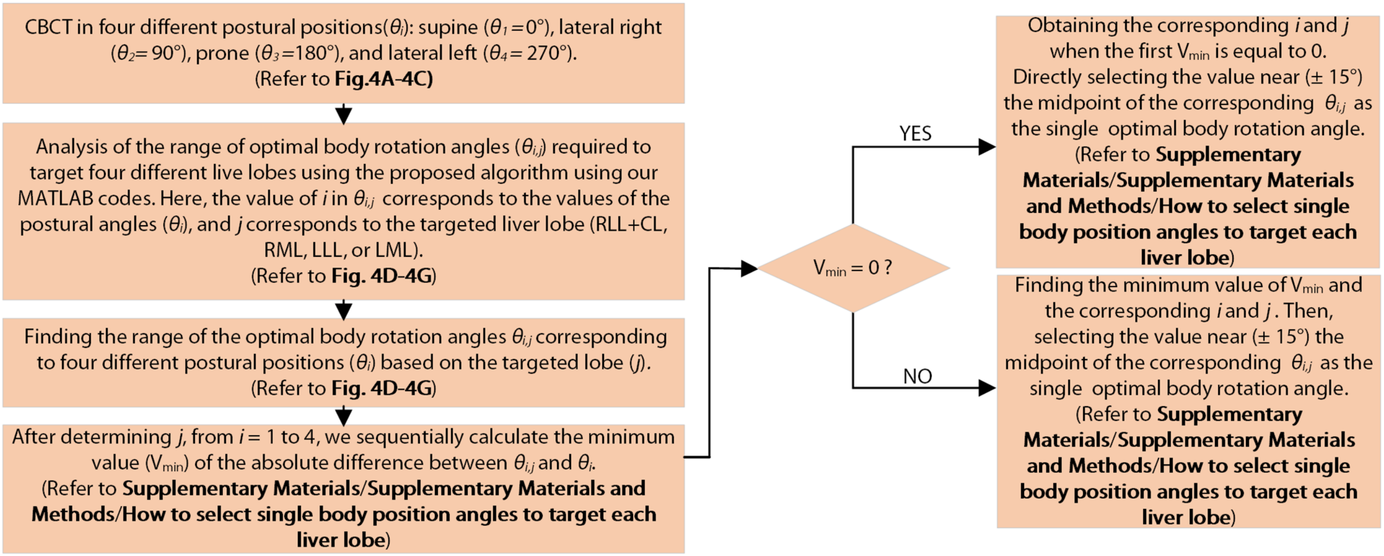

CBCT in four different postural positions(θ_i): supine ($\theta_1 = 0°$), lateral right ($\theta_2 = 90°$), prone ($\theta_3 = 180°$), and lateral left ($\theta_4 = 270°$). (Refer to **Fig.4A-4C**)

Analysis of the range of optimal body rotation angles ($\theta_{i,j}$) required to target four different live lobes using the proposed algorithm using our MATLAB codes. Here, the value of *i* in $\theta_{i,j}$ corresponds to the values of the postural angles (θ_i), and *j* corresponds to the targeted liver lobe (RLL+CL, RML, LLL, or LML). (Refer to **Fig. 4D-4G**)

Finding the range of the optimal body rotation angles $\theta_{i,j}$ corresponding to four different postural positions (θ_i) based on the targeted lobe (*j*). (Refer to **Fig. 4D-4G**)

After determining *j*, from $i = 1$ to 4, we sequentially calculate the minimum value (V_{min}) of the absolute difference between $\theta_{i,j}$ and θ_i. (Refer to **Supplementary Materials/Supplementary Materials and Methods/How to select single body position angles to target each liver lobe**)

Obtaining the corresponding *i* and *j* when the first V_{min} is equal to 0. Directly selecting the value near (± 15°) the midpoint of the corresponding $\theta_{i,j}$ as the single optimal body rotation angle. (Refer to **Supplementary Materials/Supplementary Materials and Methods/How to select single body position angles to target each liver lobe**)

Finding the minimum value of V_{min} and the corresponding *i* and *j*. Then, selecting the value near (± 15°) the midpoint of the corresponding $\theta_{i,j}$ as the single optimal body rotation angle. (Refer to **Supplementary Materials/Supplementary Materials and Methods/How to select single body position angles to target each liver lobe**)

Fig. 8. Flowchart showing how to select the single optimal body rotation angle. This figure presents a flowchart illustrating the process of selecting the single optimal body rotation angle.

0.00067 ml. A piezoresistive differential pressure transducer (MPX 5050DP, NXP USA Inc.) was placed in the actuator, and it could monitor the blood pressure changes in front of the catheter tip during balloon inflation.

Optimal body position prediction model

At vessel bifurcations, if one artery leads to the tumor and the other does not, it is necessary to facilitate particle migration through the first artery. Particles are subject to gravity because of their weight. Therefore, at the bifurcation, the MMRs naturally migrate toward the lowest artery, in other words, toward the artery with the most negative bifurcation angle (α, see Fig. 1B) with respect to the horizontal plane. α is always in the range of −90° to 90°. Here, we develop an algorithm to predict the optimal body position during microrobot navigation. After obtaining the vascular tree from CBCT, the 3D geometry of the segmented hepatic artery centerlines is extracted in the Vascular Modelling Toolkit (VMTK) library (movie S1); the algorithm stores the vascular tree as a binary tree. The root corresponds to the first division of the hepatic artery. Branch divisions are defined by their 3D bifurcation vector. The pathway to the targeted liver lobe and the number of bifurcations to cross are determined by optimizing angle below the horizontal plane for each bifurcation.

The main hepatic artery is mostly aligned in the craniocaudal direction close to the $\mathbf{B}_0$ (z axis) in the headfirst supine position, while the first and second bifurcations are more in the transverse direction and affected by the individual's rotation angle (θ) along the main hepatic artery, specifically the z axis or slice axis. Hence, the 3D rotation matrix is

$$R_z(\theta) = \begin{pmatrix} \cos\theta & -\sin\theta & 0 \\ \sin\theta & \cos\theta & 0 \\ 0 & 0 & 1 \end{pmatrix} \tag{1}$$

The individual's rotation angle (θ) can range between 0° and 359°, with 0° a supine position of the patient and with positive θ for a right-side rotation (see Fig. 4A).

An optimal rotation range of the patient (θ) is obtained if all bifurcations leading to the targeted lobe meet the following conditions

$$\alpha_{\text{Targeted}|\theta} \leq 0^\circ \text{ and } \alpha_{\text{Targeted}|\theta} \leq \alpha_{\text{Nontargeted}|\theta} \tag{2}$$

where $\alpha_{\text{Targeted}|\theta}$ is the angle between the horizontal plane and the targeted vessel branch at the vessel bifurcation (Fig. 1B), which was obtained by analyzing the 3D geometry of centerlines of the segmented hepatic arteries in MATLAB. Correspondingly, $\alpha_{\text{Nontargeted}|\theta}$ is the angle corresponding to the nontargeted vessel branch. Note that in our above conditions, we assume that targeting vessels and nontargeting vessels within a vascular branch are in the same plane, as shown in Fig. 1B. In practical operation, $\alpha_{\text{Targeted}|\theta}$ being less than $\alpha_{\text{Nontargeted}|\theta}$ is sufficient to achieve the enhanced targeting control effect with the use of gravity.

For each rotation angle range (θ), a decision tree is applied to determine whether θ is optimal. If θ is optimal, all $\alpha_{\text{Targeted}|\theta}$ values along the pathway to the tumor meet the conditions above. If θ is not optimal, we try to maximize the number of consecutive bifurcations that facilitate particle navigation to the tumor. This step provides information on the number of consecutive bifurcations that can be favored by gravity.

The operation details to obtain the range of the optimal patient positions were presented (movie S2 and the Supplementary Materials). After obtaining the range of optimal body rotation angles, we determined the single optimal body rotation angle based on the method outlined in the flowchart in Fig. 8. The existence of $V_{\min}$ here was to ensure that there is minimal rotation from the body's postural angle to the single body rotation angle, thereby reducing vascular deformation. In the Supplementary Materials, we combined Figs. 4 and 8 to explain how to obtain the single body rotation angle to target each lobe of pig #8, after obtaining the range of the optimal patient positions.

Experimental animals

All animal studies adhered to the National Institutes of Health *Guide for the Use and Care of Animals* and were conducted in accordance with the Canadian Council on Animal Care and approved by the CHUM (Centre Hospitalier de L'Universite de Montréal) Research Center's Institutional Animal Care Committee (C17014GSp). Hybrid pigs [N = 14 (7 females and 7 males), weight: 35 to 50 kg, age: 3 to 7 months] (Ferme Triporc Inc., Quebec, Canada) were enrolled. All experiments were done under general anesthesia, and the animals were euthanized at the end of the experiments. All angiography and CBCT acquisitions were performed in an experimental angiography room (Artis Q, Siemens, Forchheim, Germany). All MRN procedures were performed in a 3-T MRI scanner (Skyra, Siemens, Germany).

MMR injection in the angiography suite

The purpose of this experiment was to evaluate the MMR distribution when injected in an angiography suite without magnetic fields and aggregate formation. Two pigs had MMR injections. A 5-French introducer was placed via the femoral approach. The main hepatic artery was catheterized with a 4-French glidecath cobra catheter (Terumo, Tokyo, Japan). After a selective angiography (DSA) of the hepatic artery, selective catheterization of the gastroduodenal and left gastric arteries was performed with a 2.5-French microcatheter (Cantata, Cook Medical, Bloomington). To prevent nontarget embolization outside the liver, embolization of both arteries was performed using an experimental gel made of chitosan-sodium tetradecyl sulfate (*56*) and/or microcoils (Nester Embolization Microcoil, Cook Medical) (Fig. 4B). However, during the autopsy, we discovered that the gel had caused ulceration to the duodenum and stomach. As a result of ethical concerns raised by the veterinarians, we had to switch to coils for a safer alternative. We confirmed that no damage was observed after the change and decided to continue embolizing with coils. Then, 2000 MMRs were injected in free flow in the angiography suite. An MRI of the explanted liver was performed after the euthanasia of the two animals [T1-VIBE acquisitions, out-of-phase: repetition time (TR) = 5.2 ms, echo time (TE) = 1.4 ms; in-phase: TR = 5.2 ms, TE = 2.6 ms, flip angle (FA) = 9°, matrix size = 195 × 320, slice thickness = 3 mm, field of view (FOV) = 282 mm × 347 mm, bandwidth = 1040 Hz, slice = 72]. In all experiments, the imaging parameters of the T1-VIBE sequence were kept constant.

Preparation of MRN procedures in the angiography suite (visit 1)

The purpose of this procedure was to have a 3D assessment of the anatomy of the hepatic artery and its branch divisions to each liver segment and to determine the best pig position to favor gravity for

MRN. The 3D DSA acquisitions of the hepatic artery were performed by manual injection to localize the branch divisions of the hepatic artery. An embolization of the gastroduodenal and left gastric branches was also performed to prevent nontarget embolization in the upper gastrointestinal system.

Then, CBCT acquisitions were performed with contrast injection through the 4-French catheter positioned in the proper hepatic artery to obtain a 3D model of the liver arterial system in four different positions (0°, 90°, 180°, and 270°). In our blood vessel segmentation process from CBCT images, the reconstruction of segmented vessels was verified by referring to angiography images (Fig. 3A). It was ensured that even small vessels were visible and that vessel information, including those crucial for navigating to different liver lobes, was not lost during the segmentation process.

MMR injection in the control and navigation groups (visit 2)

For the four pigs in the control group, the cobra Glidecath catheter was placed 3 cm below the first bifurcation (left and right hepatic arteries) in preparation for aggregate injections. All control pigs were positioned in the supine position.

For the pigs in the two navigation groups, a 5-French balloon catheter (2-cm-long balloon with 6-mm inflated diameter, Powerflex P3, Cordis, USA) was positioned in the proper hepatic artery. The pigs were rotated to the optimal MRN position (Table 1) obtained by using the algorithm proposed above.

Animals were transferred to the MRI room. MRA was acquired in the coronal plane according to the arterial phase with a T1-weighted gradient-recalled sequence (TR = 3.33 ms, TE = 1.23 ms, FA = 19°, FOV = 300 mm, 0.78 mm in-plane isotropic voxel, and 0.8 mm slice thickness) under breath hold, after intravenous injection of 0.5 mmol/kg of gadolinium (Prohance, Bracco Imaging, Anjou, Quebec). The imaging has a 7-s delay after bolus tracking in the proximal abdominal aorta.

For each pig in the control group, the cobra catheter was connected to the MRI-compatible injector to allow the injection of microrobots in free flow and without navigation. For the pigs in the navigation groups, the blood flow rate in the proper hepatic artery was reduced to an appropriate range compatible with MRN. The high-precision MRI-compatible balloon inflation system was connected to the balloon inflation port of the catheter to inflate the balloon and the guidewire lumen port to monitor the blood pressure (fig. S12). The blood flow rate in the proper hepatic artery was measured using the 2D cine phase-contrast sequence (TR = 50.32 ms, TE = 3.61 ms, FA = 20°, FOV = 200 mm, voxel size = 0.39 mm by 0.39 mm by 3.70 mm) under cardiac gating and breath hold. The measurement was taken on a cross section perpendicular to the long axis of the proper hepatic artery. Flow measurements were repeated for different balloon inflation volumes until the blood flow rate was reduced to ~0.5 to 1.0 ml/s. Then, the balloon inflation port was closed, and the guidewire lumen port of the catheter was connected to the MRI-compatible injector to allow the injection of MMRs in the proper hepatic artery.

Retrospective clinical study

Clinical data and the corresponding analysis results were obtained during the period authorized by the CHUM Research Ethics Committee (20.039). The requirement for patient consent was waived by the Director of Professional Services in CHUM, given the retrospective nature of this project. In addition, the risk of this project was minimal for patients.

Statistics and data analysis

Experimental results were studied using Student’s *t* test. The difference between the control group and the two navigation groups was considered statistically significant at $P < 0.05$.

Supplementary Materials

This PDF file includes:
Supplementary Materials and Methods
Figs. S1 to S12
Tables S1 and S2
References (*57–59*)

Other Supplementary Material for this manuscript includes the following:
Movies S1 and S2
Data S1
MDAR Reproducibility Checklist

REFERENCES AND NOTES

1. P. E. Dupont, B. J. Nelson, M. Goldfarb, B. Hannaford, A. Menciassi, M. K. O’Malley, N. Simaan, P. Valdastri, G.-Z. Yang, A decade retrospective of medical robotics research from 2010 to 2020. *Sci. Robot.* **6**, eabi8017 (2021).
2. B. J. Nelson, I. K. Kaliakatsos, J. J. Abbott, Microrobots for minimally invasive medicine. *Annu. Rev. Biomed. Eng.* **12**, 55–85 (2010).
3. J. Li, X. Li, T. Luo, R. Wang, C. Liu, S. Chen, D. Li, J. Yue, S.-H. Cheng, D. Sun, Development of a magnetic microrobot for carrying and delivering targeted cells. *Sci. Robot.* **3**, eaat8829 (2018).
4. J. Li, B. Esteban-Fernández de Ávila, W. Gao, L. Zhang, J. Wang, Micro/nanorobots for biomedicine: Delivery, surgery, sensing, and detoxification. *Sci. Robot.* **2**, eaam6431 (2017).
5. J. Law, X. Wang, M. Luo, L. Xin, X. Du, W. Dou, T. Wang, G. Shan, Y. Wang, P. Song, X. Huang, J. Yu, Y. Sun, Microbotic swarms for selective embolization. *Sci. Adv.* **8**, eabm5752 (2022).
6. M. Sitti, *Mobile Microrobotics* (MIT Press, 2017).
7. C.-Y. Lee, G.-Y. Chau, C.-Y. Wei, Y. Chao, Y.-H. Huang, T.-I. Huo, M.-C. Hou, Y.-H. Su, J.-C. Wu, C.-W. Su, Surgical resection could provide better outcomes for patients with hepatocellular carcinoma and tumor rupture. *Sci. Rep.* **12**, 8343 (2022).
8. B. C. Odisio, A. Ashton, Y. Yan, W. Wei, A. Kaseb, M. J. Wallace, J. N. Vauthey, S. Gupta, A. L. Tam, Transarterial hepatic chemoembolization with 70-150 μm drug-eluting beads: Assessment of clinical safety and liver toxicity profile. *J. Vasc. Interv. Radiol.* **26**, 965–971 (2015).
9. M. He, N. Jiang, X. Yin, A. Xu, K. Mu, Conventional and drug-eluting beads transarterial chemoembolization in patients with unresectable intrahepatic cholangiocarcinoma: A systematic review and pooled analysis. *J. Cancer Res. Clin. Oncol.* **149**, 531–540 (2023).
10. R. C. Gaba, R. P. Lokken, R. M. Hickey, A. J. Lipnik, R. J. Lewandowski, R. Salem, D. B. Brown, T. G. Walker, J. E. Silberzweig, M. O. Baerlocher, A. M. Echenique, M. Midia, J. W. Mitchell, S. A. Padia, S. Ganguli, T. J. Ward, J. L. Weinstein, B. Nikolic, S. R. Dariushnia, Society of Interventional Radiology Standards of Practice Committee, Quality improvement guidelines for transarterial chemoembolization and embolization of hepatic malignancy. *J. Vasc. Interv. Radiol.* **28**, 1210–1223.e3 (2017).
11. P. Popovic, B. Stabuc, R. Jansa, M. Garbajs, Survival of patients with intermediate stage hepatocellular carcinoma treated with superselective transarterial chemoembolization using doxorubicin-loaded DC Bead under cone-beam computed tomography control. *Radiat. Oncol.* **50**, 418–426 (2016).
12. C. Tous, N. Li, I. P. Dimov, S. Kadoury, A. Tang, U. O. Häfeli, Z. Nosrati, K. Saatchi, G. Moran, M. J. Couch, S. Martel, S. Lessard, G. Soulez, Navigation of microrobots by MRI: Impact of gravitational, friction and thrust forces on steering success. *Ann. Biomed. Eng.* **49**, 3724–3736 (2021).
13. A. D. C. Fonseca, T. Kohler, D. Ahmed, Ultrasound-controlled swarmbots under physiological flow conditions. *Adv. Mater. Interfaces* **9**, 2200877 (2022).
14. R. Chen, D. Folio, A. Ferreira, Analysis and comparison of electromagnetic microrobotic platforms for biomedical applications. *Appl. Sci.* **12**, 456 (2022).
15. M. Salehizadeh, E. Diller, Three-dimensional independent control of multiple magnetic microrobots via inter-agent forces. *Int. J. Robot. Res.* **39**, 1377–1396 (2020).
16. S. Pane, V. Iacovacci, M. H. D. Ansari, A. Menciassi, Dynamic tracking of a magnetic micro-roller using ultrasound phase analysis. *Sci. Rep.* **11**, 23239 (2021).
17. A. Bigot, C. Tremblay, G. Soulez, S. Martel, Magnetic resonance navigation of a bead inside a three-bifurcation pmma phantom using an imaging gradient coil insert. *IEEE Trans. Robot.* **30**, 719–727 (2014).
18. S. Martel, J.-B. Mathieu, O. Felfoul, A. Chanu, E. Aboussouan, S. Tamaz, P. Pouponneau, L. H. Yahia, G. Beaudoin, G. Soulez, M. Mankiewicz, Automatic navigation of an untethered device in the artery of a living animal using a conventional clinical magnetic resonance imaging system. *Appl. Phys. Lett.* **90**, 114105 (2007).

19. K.-H. Lee, E. Liapi, J. A. Vossen, M. Buijs, V. P. Ventura, C. Georgiades, K. Hong, I. Kamel, M. S. Torbenson, J.-F. H. Geschwind, Distribution of iron oxide-containing Embosphere particles after transcatheter arterial embolization in an animal model of liver cancer: Evaluation with MR imaging and implication for therapy. *J. Vasc. Interv. Radiol.* **19**, 1490–1496 (2008).
20. S. Jeon, S. Kim, S. Ha, S. Lee, E. Kim, S. Y. Kim, S. H. Park, J. H. Jeon, S. W. Kim, C. Moon, B. J. Nelson, J.-Y. Kim, S.-W. Yu, H. Choi, Magnetically actuated microrobots as a platform for stem cell transplantation. *Sci. Robot.* **4**, eaav4317 (2019).
21. G. Go, A. Yoo, K. T. Nguyen, M. Nan, B. A. Darmawan, S. Zheng, B. Kang, C.-S. Kim, D. Bang, S. Lee, K.-P. Kim, S. S. Kang, K. M. Shim, S. E. Kim, S. Bang, D.-H. Kim, J.-O. Park, E. Choi, Multifunctional microrobot with real-time visualization and magnetic resonance imaging for chemoembolization therapy of liver cancer. *Sci. Adv.* **8**, eabq8545 (2022).
22. Z. Wu, L. Li, Y. Yang, P. Hu, Y. Li, S.-Y. Yang, L. V. Wang, W. Gao, A microrobotic system guided by photoacoustic computed tomography for targeted navigation in intestines in vivo. *Sci. Robot.* **4**, eaax0613 (2019).
23. D. Li, C. Liu, Y. Yang, L. Wang, Y. Shen, Micro-rocket robot with all-optic actuating and tracking in blood. *Light Sci. Appl.* **9**, 84 (2020).
24. V. M. Jooss, J. S. Bolten, J. Huwyler, D. Ahmed, In vivo acoustic manipulation of microparticles in zebrafish embryos. *Sci. Adv.* **8**, eabm2785 (2022).
25. J. Yu, D. Jin, K.-F. Chan, Q. Wang, K. Yuan, L. Zhang, Active generation and magnetic actuation of microrobotic swarms in bio-fluids. *Nat. Commun.* **10**, 5631 (2019).
26. E. Kim, S. Jeon, H.-K. An, M. Kianpour, S.-W. Yu, J.-Y. Kim, J.-C. Rah, H. Choi, A magnetically actuated microrobot for targeted neural cell delivery and selective connection of neural networks. *Sci. Adv.* **6**, eabb5696 (2020).
27. A. Ramos-Sebastian, S. J. Gwak, S. H. Kim, Multimodal locomotion and active targeted thermal control of magnetic agents for biomedical applications. *Adv. Sci.* **9**, 2103863 (2022).
28. D. Son, M. C. Ugurlu, M. Sitti, Permanent magnet array–driven navigation of wireless millirobots inside soft tissues. *Sci. Adv.* **7**, eabi8932 (2021).
29. Q. Wang, K. F. Chan, K. Schweizer, X. Du, D. Jin, S. C. H. Yu, B. J. Nelson, L. Zhang, Ultrasound Doppler-guided real-time navigation of a magnetic microswarm for active endovascular delivery. *Sci. Adv.* **7**, eabe5914 (2021).
30. M. Gräser, F. Thieben, P. Szwargulski, F. Werner, N. Gdaniec, M. Boberg, F. Griese, M. Möddel, P. Ludewig, D. van de Ven, O. M. Weber, O. Woywode, B. Gleich, T. Knopp, Human-sized magnetic particle imaging for brain applications. *Nat. Commun.* **10**, 1936 (2019).
31. N. Li, F. Michaud, Z. Nosrati, D. Loghin, C. Tremblay, R. Plantefève, K. Saatchi, U. O. Häfeli, S. Martel, G. Soulez, MRI-compatible injection system for magnetic microparticle embolization. *IEEE Trans. Biomed. Eng.* **66**, 2331–2340 (2018).
32. P. Pouponneau, J.-C. Leroux, G. Soulez, L. Gaboury, S. Martel, Co-encapsulation of magnetic nanoparticles and doxorubicin into biodegradable microcarriers for deep tissue targeting by vascular MRI navigation. *Biomaterials* **32**, 3481–3486 (2011).
33. N. Li, thesis, Ecole Polytechnique, Montreal, Canada (2019).
34. F. Michaud, N. Li, R. Plantefève, Z. Nosrati, C. Tremblay, K. Saatchi, G. Moran, A. Bigot, U. O. Häfeli, S. Kadoury, A. Tang, P. Perreault, S. Martel, G. Soulez, Selective embolization with magnetized microbeads using magnetic resonance navigation in a controlled-flow liver model. *Med. Phys.* **46**, 789–799 (2019).
35. Q. Fan, C. Eichner, M. Afzali, L. Mueller, C. M. W. Tax, M. Davids, M. Mahmutovic, B. Keil, B. Bilgic, K. Setsompop, H.-H. Lee, Q. Tian, C. Maffei, G. Ramos-Llordén, A. Nummenmaa, T. Witzel, A. Yendiki, Y.-Q. Song, C.-C. Huang, C.-P. Lin, N. Weiskopf, A. Anwander, D. K. Jones, B. R. Rosen, L. L. Wald, S. Y. Huang, Mapping the human connectome using diffusion MRI at 300 mT/m gradient strength: Methodological advances and scientific impact. *Neuroimage* **254**, 118958 (2022).
36. Z. Nosrati, N. Li, F. Michaud, S. Ranamukhaarachchi, S. Karagiozov, G. Soulez, S. Martel, K. Saatchi, U. O. Häfeli, Development of a coflowing device for the size-controlled preparation of magnetic-polymeric microspheres as embolization agents in magnetic resonance navigation technology. *ACS Biomater Sci. Eng.* **4**, 1092–1102 (2018).
37. L. A. da Silveira, F. B. C. Silveira, V. P. S. Fazan, Arterial diameter of the celiac trunk and its branches: Anatomical study. *Acta Cir. Bras.* **24**, 43–47 (2009).
38. L. Mellal, K. Belharet, D. Folio, A. Ferreira, Optimal structure of particles-based superparamagnetic microrobots: Application to MRI guided targeted drug therapy. *J. Nanopart. Res.* **17**, 64 (2015).
39. R. Kikinis, S. D. Pieper, K. G. Vosburgh, 3D Slicer: A platform for subject-specific image analysis, visualization, and clinical support, in *Intraoperative Imaging and Image-Guided Therapy* (Springer, 2014), pp. 277–289.
40. N. A. Michels, Newer anatomy of the liver and its variant blood supply and collateral circulation. *Am. J. Surg.* **112**, 337–347 (1966).
41. P. Pouponneau, G. Bringout, S. Martel, Therapeutic magnetic microcarriers guided by magnetic resonance navigation for enhanced liver chemoembilization: A design review. *Ann. Biomed. Eng.* **42**, 929–939 (2014).
42. C. D. Malone, A. Banerjee, M. T. Alley, S. S. Vasanawala, A. C. Roberts, A. Hsiao, Pelvic blood flow predicts fibroid volume and embolic required for uterine fibroid embolization: A pilot study with 4D flow MR angiography. *AJR Am. J. Roentgenol.* **210**, 189–200 (2018).
43. R. F. Hanna, V. Z. Miloushev, A. Tang, L. A. Finklestone, S. Z. Brejt, R. S. Sandhu, C. S. Santillan, T. Wolfson, A. Gamst, C. B. Sirlin, Comparative 13-year meta-analysis of the sensitivity and positive predictive value of ultrasound, CT, and MRI for detecting hepatocellular carcinoma. *Abdom. Radiol.* **41**, 71–90 (2016).
44. N. Li, C. Tous, I. P. Dimov, D. Cadoret, P. Fei, Y. Majedi, S. Lessard, Z. Nosrati, K. Saatchi, U. O. Häfeli, A. Tang, S. Kadoury, S. Martel, G. Soulez, Quantification and 3D localization of magnetically navigated superparamagnetic particles using MRI in phantom and swine chemoembolization models. *IEEE Trans. Biomed. Eng.* **69**, 2616–2627 (2022).
45. T. De Baere, P. Mariani, Surgical or percutaneous hepatic artery cannulation for chemotherapy. *J. Visc. Surg.* **151** (Suppl. 1), S17–S20 (2014).
46. J. S. Weinstein, C. G. Varallyay, E. Dosa, S. Gahramanov, B. Hamilton, W. D. Rooney, L. L. Muldoon, E. A. Neuwelt, Superparamagnetic iron oxide nanoparticles: Diagnostic magnetic resonance imaging and potential therapeutic applications in neurooncology and central nervous system inflammatory pathologies, a review. *J. Cereb. Blood Flow Metab.* **30**, 15–35 (2010).
47. V. Iacovacci, G. Lucarini, L. Ricotti, P. Dario, P. E. Dupont, A. Menciassi, Untethered magnetic millirobot for targeted drug delivery. *Biomed. Microdevices* **17**, 63 (2015).
48. S. Palagi, B. Mazzolai, C. Innocenti, C. Sangregorio, L. Beccai, How does buoyancy of hydrogel microrobots affect their magnetic propulsion in liquids? *Appl. Phys. Lett.* **102**, 124102 (2013).
49. N. LI, C. Tous, P. Fei, I. P. Dimov, S. Lessard, U. O. Hafali, S. Martel, A. Tang, G. Soulez, *U-Net-Based Deep Convolutional Neural Network for Detection of Superparamagnetic Drug-Eluting Particles Used for Liver Chemoembolization* (ISMRM, 2022).
50. T. Bomberna, G. A. Koudehi, C. Claerebout, C. Verslype, G. Maleux, C. Debbaut, Transarterial drug delivery for liver cancer: Numerical simulations and experimental validation of particle distribution in patient-specific livers. *Expert Opin. Drug Deliv.* **18**, 409–422 (2021).
51. A. Ntonas, A. Katsourakis, N. Galanis, E. Filo, G. Noussios, Comparative anatomical study between the human and swine liver and its importance in xenotransplantation. *Cureus* **12**, e9411 (2020).
52. L. M. Pak, N. E. Kemeny, M. Capanu, J. F. Chou, T. Boucher, A. Cercek, V. P. Balachandran, T. P. Kingham, P. J. Allen, R. P. DeMatteo, W. R. Jarnagin, M. I. D'Angelica, Prospective phase II trial of combination hepatic artery infusion and systemic chemotherapy for unresectable colorectal liver metastases: Long term results and curative potential. *J. Surg. Oncol.* **117**, 634–643 (2018).
53. A. G. Duffy, S. V. Ulahannan, O. Makorova-Rusher, O. Rahma, H. Wedemeyer, D. Pratt, J. L. Davis, M. S. Hughes, T. Heller, M. ElGindi, A. Uppala, F. Korangy, D. E. Kleiner, W. D. Figg, D. Venzon, S. M. Steinberg, A. M. Venkatesan, V. Krishnasamy, N. Abi-Jaoudeh, E. Levy, B. J. Wood, T. F. Greten, Tremelimumab in combination with ablation in patients with advanced hepatocellular carcinoma. *J. Hepatol.* **66**, 545–551 (2017).
54. P. Bize, R. Duran, K. Fuchs, O. Dormond, J. Namur, L. A. Decosterd, O. Jordan, E. Doelker, A. Denys, Antitumoral effect of sunitinib-eluting beads in the rabbit VX2 tumor model. *Radiology* **280**, 425–435 (2016).
55. K. Fuchs, P. E. Bize, O. Dormond, A. Denys, E. Doelker, G. Borchard, O. Jordan, Drug-eluting beads loaded with antiangiogenic agents for chemoembolization: In vitro sunitinib loading and release and in vivo pharmacokinetics in an animal model. *J. Vasc. Interv. Radiol.* **25**, 379–387.e372 (2014).
56. F. Zehtabi, V. Dumont-Mackay, A. Fatimi, A. Bertrand-Grenier, H. Héon, G. Soulez, S. Lerouge, Chitosan–sodium tetradecyl sulfate hydrogel: Characterization and preclinical evaluation of a novel sclerosing embolizing agent for the treatment of endoleaks. *Cardiovasc. Intervent. Radiol.* **40**, 576–584 (2017).
57. N. Li, C. Tremblay, S. Martel, Combining oscillating flow and clinical MRI gradients for targeted therapy, in *2017 International Conference on Manipulation, Automation and Robotics at Small Scales (MARSS)* (IEEE, 2017), pp. 1–4.
58. M. C. Mascolo, Y. Pei, T. A. Ring, Room temperature co-precipitation synthesis of magnetite nanoparticles in a large pH window with different bases. *Materials* **6**, 5549–5567 (2013).
59. M. Lecouvey, I. Mallard, T. Bailly, R. Burgada, Y. Leroux, A mild and efficient one-pot synthesis of 1-hydroxymethylene-1, 1-bisphosphonic acids. Preparation of new tripod ligands. *Tetrahedron Lett.* **42**, 8475–8478 (2001).

Acknowledgments

Funding: This work was supported by the Natural Sciences and Engineering Research Council of Canada (CHRP 478474-15), the Canadian Institutes of Health Research (grant nos. CPG-140179 and PJT-173319), Fonds de recherche du Québec en Santé (FRQ-S) and Fondation de l'association des radiologistes du Québec (FARQ) Clinical Research Scholarship–Senior Salary Award (FRQS-ARQ #298509), the National Natural Science Foundation of China (61973207), the Shang-hai High-End Foreign Expert Project (23WZ2503000), and the Shanghai Rising-Star Program (20QA1403900).

Author contributions: G.S. and S.M. contributed to the conceptualization of the project, supervised the project, and provided project administration support. N.L., P.F., C. Tous, C. Tremblay, S.M., and G.S. contributed to the development of the methodology. Z.N., C.N.N., K.S., and U.O.H. were involved in the synthesis of particles. N.L. and Q.Z. contributed to the system design. C. Tous was responsible for the development of the navigation software. I.O. and P.F. led the code software development, particularly in creating the vascular centerline extraction and Matlab code. N.L., P.F., C. Tous, M.R.A., I.P.D., M.-L.H., A.H., S.L., and G.S. were involved in conducting the experiments. N.L., P.F., M.-L.H., and G.S. contributed to the analysis of the results. I.O. and G.S. performed the analysis of clinical data. S.M., Q.Z., A.T., and G.S. were responsible for acquiring funding for the project. N.L. contributed to the writing of the original draft. All authors participated in the review and editing of the manuscript. **Competing interests:** G.S., N.L., C. Tous, I.P.D., P.F., and S.M. filed a US patent application (no. 63/620,011) for the study in the paper. All other authors declare that they have no competing financial interests. **Data and materials availability:** All data needed to evaluate the conclusions in the paper are present in the paper. The codebase and dataset of the work can be found at https://doi.org/10.5281/zenodo.10503774.

Submitted 29 March 2023
Accepted 17 January 2024
Published 14 February 2024
10.1126/scirobotics.adh8702

Science Robotics

Human-scale navigation of magnetic microrobots in hepatic arteries

Ning Li, Phillip Fei, Cyril Tous, Mahdi Rezaei Adariani, Marie-Lou Hautot, Inès Ouedraogo, Amina Hadjadj, Ivan P. Dimov, Quan Zhang, Simon Lessard, Zeynab Nosrati, Courtney N. Ng, Katayoun Saatchi, Urs O. Häfeli, Charles Tremblay, Samuel Kadoury, An Tang, Sylvain Martel, and Gilles Soulez

Sci. Robot. **9** (87), eadh8702. DOI: 10.1126/scirobotics.adh8702

Editor's summary

Magnetic microrobots can be used for selective drug delivery in arteries; however, challenges from gravity and blood flow can make it difficult to navigate them with accuracy. Li *et al.* developed an algorithm to determine the optimal patient position such that gravity helps, rather than hinders, targeted drug delivery in hepatic arteries. Magnetic fields generated from MRI were used to steer the microrobots through hepatic arteries to targeted liver lobes in living pigs. When the algorithm was used to determine the optimal position for the pig, the number of microrobots that reach targeted lobes increased up to 2.6-fold compared with microrobots navigated in pigs that were not repositioned. Finding the optimal patient position could improve efficiency in drug-delivery techniques that rely on an external field for navigation. —Melisa Yashinski

Science Robotics (ISSN 2470-9476) is published by the American Association for the Advancement of Science. 1200 New York Avenue NW, Washington, DC 20005. The title *Science Robotics* is a registered trademark of AAAS.